Microstructure and Mechanical Properties of a Precipitation-Strengthened Fe–Al–Nb Alloy

Sarper Nizamoglu, Angelika Gedsun, Alexander Kauffmann,* Michael Ghosh, Heiner Michels, Tim Groten, Camelia Schulz, Christoph Breuner, Sascha Seils, Daniel Schliephake, Stephan Laube, Martin Palm, and Martin Heilmaier

Fe–Al alloys provide an attractive property profile for applications at temperatures of up to 700 °C. Herein, a Fe–25Al–2Nb (at%) alloy is, manufactured on an application-relevant scale. Preforms are cast and subsequently forged into a turbine blade shape. The microstructural evolution and mechanical properties, namely quasistatic strength and creep response, are tested in different manufacturing conditions and are compared to the properties of equilibrated laboratory alloys, as well as to literature results. The cast process leads to coarse-grained initial nonequilibrium microstructures with lower amounts of Laves phase as compared to thermodynamic equilibrium. Forging at 900 °C leads to the significant formation of subgrains in the Fe–Al matrix and precipitation of the Laves phase. The as-cast condition of Fe–25Al–2Nb exhibits a complex creep behavior governed by the transient formation of a coherent Heusler phase as well as Laves phase formation and recrystallization in later stages of creep. In the forged condition, the material behaves similarly to long-term annealed material. Although Fe–25Al–2Nb has slightly lower strength and lower creep resistance over the entire temperature range tested, it performs well compared to Ta-containing Fe–Al alloys due to its lower cost and density.

1. Introduction

Iron aluminides are attractive materials for structural applications at high temperatures, e.g., for blades for stationary turbines, because of their low density, good corrosion and wear resistance, and low costs. Moreover, no or only small concentrations of strategic elements are needed, and the materials can be produced by standard processing techniques such as casting, rolling, and forging.[1–3] Fe–Al-based alloys are, therefore, being considered to replace Cr-containing steels and possibly also polycrystalline Ni-based superalloys as high-temperature structural materials for certain applications.[4] However, mechanical properties such as creep resistance, yield strength above 500 °C, and ductility at room temperature (RT) still need to be improved. Thus, only niche applications as bulk structural material are reported so far.[5] Consequently, several alloying concepts focusing on, e.g., coherent or incoherent intermetallic precipitates, carbides or borides, solid solution strengthening, or ordering have been employed over the years to develop new iron aluminide alloys with improved properties.[5–7]

Strengthening by incoherent Laves phase precipitates in Fe–Al–X (X = Ti, Zr, Nb, Ta)[8–10] and more complex multicomponent Fe–Al alloys is promising when the brittle Laves phase precipitates are fine and homogeneously distributed in the matrix. In Fe–Al–Ta with Al contents close to 25 at.% (D0$_3$-ordered at RT), this can be achieved by means of heat treatment, thermo-mechanical treatment, and doping with B where the precipitation of the Laves phase is preceded by precipitation of a metastable Heusler phase.[11–13] The formation of the Laves phase is kinetically retarded, and it, therefore, preferably nucleates at grain

S. Nizamoglu, A. Kauffmann, C. Schulz, C. Breuner, S. Seils,
D. Schliephake, S. Laube, M. Heilmaier
Institute for Applied Materials (IAM-WK)
Karlsruhe Institute of Technology (KIT)
Engelbert-Arnold-Str. 4, Karlsruhe D-76131, Germany
E-mail: alexander.kauffmann@kit.edu

The ORCID identification number(s) for the author(s) of this article can be found under https://doi.org/10.1002/adem.202300148.

A. Gedsun, M. Palm
Max-Planck-Institut für Eisenforschung GmbH
Max-Planck-Str. 1, Düsseldorf D-40237, Germany

A. Kauffmann
Karlsruhe Nano Micro Facility (KNMFi)
Karlsruhe Institute of Technology (KIT)
Hermann-von-Helmholtz-Platz 1, Eggenstein-Leopoldshafen D-76344, Germany

M. Ghosh, H. Michels
Access e.V.
Intzestraße 5, Aachen D-52072, Germany

T. Groten
Leistritz Turbinentechnik GmbH
Lempstraße 24, Remscheid D-42859, Germany

**ADVANCED
SCIENCE NEWS**

www.advancedsciencenews.com

**ADVANCED
ENGINEERING
MATERIALS**

www.aem-journal.com

boundaries in the beginning and only in later stages homogeneously within grains.[14] Hence, additional nucleation sites like subgrain boundaries and borides can lead to a more homogeneous distribution of the Laves phase in the Fe–Al matrix.

In Fe–Al–Ta, Heusler phase precipitates increase strength and creep resistance up to 800 °C.[13] The creep strength does not decrease when the metastable Heusler phase dissolves, but it is compensated by precipitation of the Laves phase and solid solution strengthening of the Fe–Al matrix.[12] Also, in Fe–Al–Nb, the formation of the Laves phase is preceded by the formation of the metastable Heusler phase[8,9,15] when the Fe–Al matrix is supersaturated in Nb, for example, upon cooling. Regarding further assessments and informations on phase equilibria in the Fe–Al-rich part of this particular system, the reader is referred to refs.[16–20] It has been observed that Heusler phase formation during quasistatic compressive deformation at temperatures close to 750 °C[8] leads to a slight increase in yield strength. However, solid solution strengthening was found to be the main strengthening mechanism since Laves phase precipitates are too coarse and Heusler phase forms only within a limited temperature range, from 600 °C (observed after 100 h) up to 700 °C (observed after 10 h). The addition of B accelerates the dissolution of the Heusler phase and precipitation of the stable Laves phase[21] (for Fe–Al–Ta, see also[12]), however not in the alloys[22] that are investigated in the present publication, possibly because of the low concentration of B. Specifically, Heusler phase formed in Fe–24.4Al–2Nb–0.03B (all compositions in the article are provided in at.% unless otherwise noted). It dissolved after heat treatment at 700 °C/100 h,[20] giving rise to a more even distribution of Laves phase precipitates in the matrix. However, no improvement in yield strength was observed compared to alloys with less evenly distributed Laves phase precipitates or higher Al content. A slightly higher yield strength was obtained in alloys with higher Al contents due to enhanced solubility of Nb in the Fe–Al matrix and thus improved solid solution strengthening. Doping with B showed no effect on the microstructure at higher Al contents and has, therefore, no effect on the compressive yield strength.[23]

The present study aims at understanding the strengthening and deformation mechanisms in Fe–Al–Nb alloys for the production of steam turbine blades intended to be used at temperatures up to 700 °C. Samples in the cast and forged condition were taken from different regions of the industrially manufactured parts and blades. Specifically, the yield strength and creep behavior are correlated to the formed Laves or Heusler phase and microstructural changes after different heat treatments and forging. The results are compared to those of reference alloys produced on a laboratory scale and to results from an established Fe-Al-Ta alloy with the same Al and comparable Ta content, which serves as a benchmark.

2. Experimental Section

The alloy with a nominal composition of Fe–25Al–2Nb was cast into preforms by gravity casting. The preforms were designed to be forged into turbine blades in the following production steps. Melting was performed using two different casting methods and devices: 1) casting under vacuum (<0.4 mbar) was performed using a Leicomelt (Leybold Induction Cold Melting, ALD Vacuum Technologies, Hanau, Germany) device. The melt was superheated to around 1520 °C and then poured through a funnel and runner into the preheated mold. Cooling inside the mold was done in air and 2) Another batch of material was synthesized in a roll-over furnace while continuously rinsing the setup with Ar. At about 1505 °C, the roll-over sequence was started by turning about 180° within 7 s, and the melt was poured through the runner into the mold. Again, the samples cooled down while exposed to air. No significant differences in microstructure and mechanical properties were obtained for the two successful casting procedures. Hence, they are not further differentiated in what follows.

Forging was performed in a uniaxial, energy-controlled (no distinct strain rate to be obtained) screw press after 30 min of soaking in the air at 900 or 1050 °C with maximum true strains of 0.5 ("root" section in **Figure 1**a) up to 2.0 ("head" section in Figure 1b). Handling of the samples from the soaking furnace to forging was in the tens of seconds range. Focus of the present study was on material forged at 900 °C.

Reference samples of nominally the same composition were obtained by vacuum induction melting under argon on a laboratory scale. The alloys were cast into a rectangular cold copper mold of about $200 \times 40 \times 180 \, mm^3$.

The samples for microstructural and mechanical analysis of the industrial scale manufacturing were machined from two different positions of both preforms and blades by electrical discharge machining (EDM); see Figure 1 for cutting positions labeled "head," "sprue," and "root," respectively. To investigate the possible effect of increased vacancy concentration from rapid cooling, as it is well known to occur in Fe–Al-based alloys,[24,25] some samples from both batches in the as-cast state were annealed for 168 h at 400 °C in air in a box furnace and subsequently furnace-cooled. A minimum vacancy concentration can be achieved by this treatment. Heat treatments by induction heating to emulate the thermal profile during the compression tests were performed in the mechanical testing machine using the same temperature profile as during the compression tests but
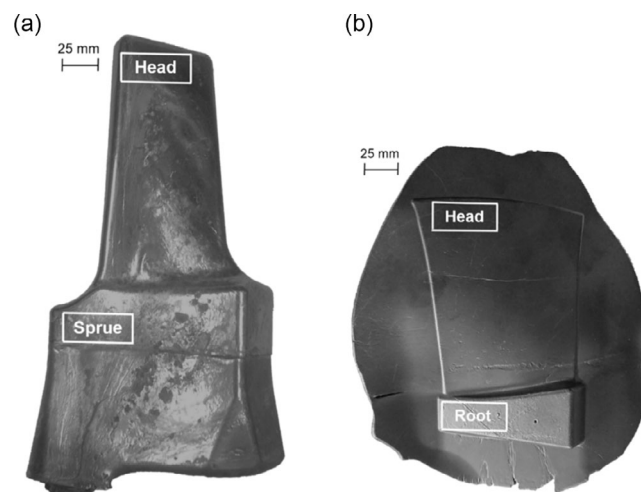

Figure 1. Photographs of (a) a cast preform and (b) a forged turbine blade. Positions, where the samples were extracted, are labeled.

**ADVANCED
SCIENCE NEWS**

www.advancedsciencenews.com

**ADVANCED
ENGINEERING
MATERIALS**

www.aem-journal.com

without load. The heat treatment duration is approximately 30 min. 1000 h of annealing at 700 °C was performed under Ar atmosphere with Ti getter in a tube furnace. The cast blocks of the laboratory reference samples were equilibrated for 1000 h at 700 °C and additionally for 168 h at 400 °C to reduce the vacancy concentration for mechanical testing at RT.

Quasistatic compression tests at an initial strain rate of $\dot{\varepsilon} = 10^{-4}\,\mathrm{s}^{-1}$ and temperatures between RT and 1050 °C on the industrial scale manufactured Fe–25Al–2Nb were performed using an electro-mechanical universal testing machine Zwick 1478 (ZwickRoell AG, Ulm, Germany) equipped with an induction heating system. Temperature was detected at the sample center. Cylindrical samples of 3 and 5 mm in diameter and length, respectively, were used. The surfaces in contact with the compression punches were ground to grit P2500 using SiC paper and lubricated with BN prior to testing. Compression creep tests on specimens from the head section of the cast preforms (Figure 1a) and the head section of the blade forged at 900 °C (Figure 1b) was conducted at 700 °C with constant engineering stress in laboratory air using the same sample geometry and testing machine. Engineering strain ε_e, strain rate $\dot{\varepsilon}_e$ and stress σ_e were converted to true quantities ε_t, $\dot{\varepsilon}_t$, and σ_t using the following formulas:

$$\sigma_t = \sigma_e(1 + \varepsilon_e) \tag{1}$$

$$\varepsilon_t = \ln(1 + \varepsilon_e) \tag{2}$$

$$\dot{\varepsilon}_t = \frac{\dot{\varepsilon}_e}{1 + \varepsilon_e} \tag{3}$$

Assuming a power law for creep with constant parameters A and n throughout the test

$$\dot{\varepsilon}_t = A \cdot \sigma_t^n \tag{4}$$

the engineering creep rate $\dot{\tilde{\varepsilon}}_e$ under constant load can be converted to a true creep rate $\dot{\tilde{\varepsilon}}_t$ under fictive constant true stress

$$\dot{\tilde{\varepsilon}}_t = \frac{\dot{\tilde{\varepsilon}}_e}{(1 + \tilde{\varepsilon}_e)^{n+1}} \tag{5}$$

For the transient creep regime $\varepsilon_t \ll 0.025$, the power law in **Equation (4)** may not be accurate, but the transform of engineering to true quantities remains small, e.g., $\varepsilon_e - \varepsilon_t \ll 3.1 \times 10^{-4}$. Hence, the impact of an inaccurate stress exponent n can be neglected. In the later stages $\varepsilon_t > 0.1$, the transfer from engineering to true quantities is significant ($\varepsilon_e - \varepsilon_t > 5.3 \times 10^{-3}$) and the parameters of the creep law do *not* change significantly as the steady state is close/achieved. The apparent stress exponents n were approximated from the engineering strain rates $\dot{\tilde{\varepsilon}}_e$. The changes in n due to the aforementioned conversion are insignificant within ±0.1. Cylindrical samples of the laboratory reference alloy with 10 and 5 mm in height and diameter, respectively, were also cut by EDM and used for compression tests. Furthermore, flat tensile specimens of 30 mm gauge length and 2 mm thickness were used. Both types of mechanical tests were performed on a Zwick 100 (ZwickRoell AG, Ulm, Germany) at an initial strain rate of $\dot{\varepsilon} = 10^{-4}\,\mathrm{s}^{-1}$. Creep tests

in tension under static load and constant temperature were performed on samples of 40 mm length, a gauge length of 24 mm, and a gauge diameter of 2 mm.

Sample preparation for microstructural analysis by scanning electron microscopy (SEM) was carried out by a standard metallographic procedure, including SiC grinding down to grit P4000. Polishing was performed using 3 and 1 µm diamond polishing suspension. A stabilized silica suspension by Buehler at pH = 9.8 was used for final polishing. SEM investigations were performed by utilizing Zeiss EVO 50, Zeiss Leo 1530, and Zeiss Ultra 55 instruments (all Carl Zeiss AG, Oberkochen, Germany). Backscattered electron contrast (BSE) imaging was conducted at 20 kV. The areal fractions of the Laves phase were determined by pixel counting following an appropriate binarization of BSE images. By assuming isotropy and isometry of the microstructures, the areal fractions were considered equal to the volume fractions. Chemical compositions were determined by energy dispersive X-ray spectroscopy (EDS) on SEM equipped with Thermofisher 6751 SDD (Thermo Fisher Scientific Inc., Waltham, MA, USA) at 20 kV or Oxford X-Max^N 150 (Oxford Instruments, Abingdon, UK) at 15 kV. Orientation imaging by electron backscatter diffraction (EBSD) was performed using an EDAX DigiView camera system (Ametek Materials Analysis Division, Mahwah, NJ, USA). As EBSD was performed in scan mode, discrimination of the ordering states of the Fe–Al is impossible, and it was indexed disordered A2 (Strukturbericht designation). Wet-chemical analysis was performed using PerkinElmer (Waltham, MA, USA) inductively coupled plasma optical emission spectroscopy setup using established standards (including B, see, for example, also more elaborated studies with varying B contents[20,22,23] which was specifically not the scope of the present investigation). An overview about all alloy compositions and processing conditions investigated in this study or taken from literature is found in **Table 1**.

3. Results and Discussion

3.1. Microstructures Subsequent to Casting and Forging

EDS was performed on the samples cut from the sprue of the industrially cast preforms. Maximum deviations from the desired chemical composition of Fe–25Al–2Nb determined on several cast products are −1.4 and +0.2 at.% for Al and Nb, respectively. The latter is well within the accuracy of EDS, while the deficit in Al seems reasonable due to preferential evaporation during the processing of the liquid. This is within acceptable tolerance for manufacturing on an industrial scale. The compositions of the laboratory reference alloys were established by wet-chemical analysis as Fe–25.7Al–2Nb and Fe–25.7Al–2Nb–0.01B.

The microstructure of the as-cast state of the industrially manufactured Fe–25Al–2Nb from the blade part of the preform shape, as shown in **Figure 2**a, consists of two phases: the polycrystalline Fe–Al matrix (dark grey levels) and Laves phase precipitates (bright gray level). It is noted that the Fe–Al matrix solidifies as disordered A2 (Strukturbericht designation), becomes B2-ordered at 900 °C and D0$_3$-ordered at about 580 °C during cooling in the composition range of the alloys discussed in this article.[20] In what follows, the matrix of Fe–25Al–2Nb is

**ADVANCED
SCIENCE NEWS**

www.advancedsciencenews.com

**ADVANCED
ENGINEERING
MATERIALS**

www.aem-journal.com

Table 1. Overview of the alloy designations used in this article in the different processing conditions and the sections discussing their properties.

Alloy designation	Processing				Section
	Scale/reference	Casting	Working	Heat treatments	
Fe–25Al–2Nb	Industrial scale	Gravity casting	–	–	3.1–3.3
			–	700 °C/1000 h	3.1, 3.3
			Forging 900°C	–	3.1–3.3
			Forging 900°C	700 °C/1000 h	3.1
Fe–25.7Al–2Nb Fe-25.7Al–2Nb-0.01B	Laboratory reference		–	700 °C/1000 h & 400 °C/168 h	3.2, 3.3
Fe–25Al–2Ta	Refs.[13,14]	Levitation melting and gravity casting	–	1000 °C/200 h	3.2, 3.3
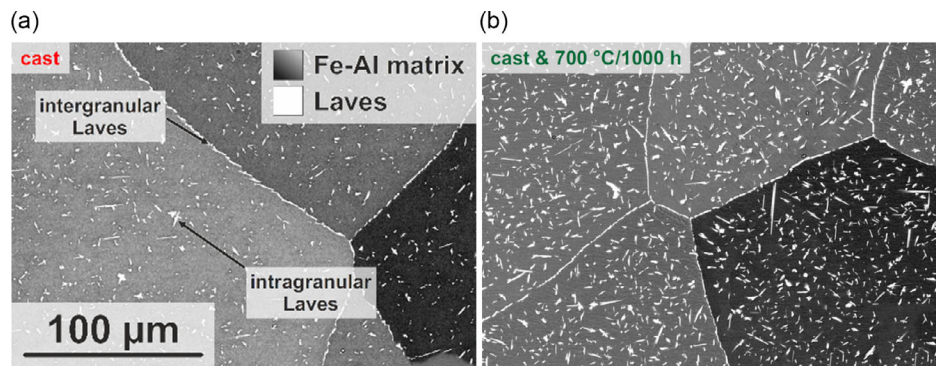
Figure 2. SEM-BSE micrographs of Fe-25Al-2Nb: (a) cast microstructure (head section in Figure 1a) and (b) microstructure of cast material subjected to additional 700 °C/1000 h (also head section). Dark gray levels indicate the Fe–Al matrix. Differences in gray levels are due to different crystal orientations. The Laves phase is seen as bright spherical and lenticular particles. The micrographs were taken at the same magnification.

referred to as the Fe–Al matrix regardless of the ordering condition. The Laves phase is C14 according to the EBSD results of the present work and consistent with the literature.[17]

The Fe–Al matrix exhibits significant orientation contrast due to electron channeling being indicative of defect-lean surface preparation. The average grain sizes of the Fe–Al matrix are coarse, between 280 and 550 μm, with a tendency to form slightly smaller grains in the head section of the preforms, possibly due to higher cooling rates in these regions. The Laves phase occurs in inter- and intragranular morphology at volume fractions of (2.6 ± 0.9) to (4.6 ± 0.9) vol% following the trend of higher cooling rate (less formation of Laves phase) in the head sections. Intergranular, chain-like Laves phase is found on practically all grain boundaries of the Fe–Al matrix phase. The intragranular Laves phase exhibits a lenticular shape at rather high aspect ratios. A specific focus of the following experiments was on samples containing (2.6 ± 0.9) vol% Laves phase.

Long-term annealing of the as-cast condition of Fe–25Al–2Nb at 700 °C (B2-ordered at heat treatment temperature[20]) for 1000 h leads to significant precipitation of Laves phase (Figure 2b). A volume fraction of (8.8 ± 0.9) vol% is found. Decoration of the grain boundaries and grain size of the Fe–Al matrix remains unaltered. The Laves phase exhibits a lenticular shape of a high aspect ratio at a size of up to 50 μm (long axis). The microstructure of the laboratory reference alloys shows less precipitates in the as-cast condition due to the higher

cooling rate in the cold copper mold, but the same distribution of the Laves phase along the grain boundaries and inside the grains after the 700 °C/1000 h heat treatment.[20]

The microstructure of the forged condition of Fe–25Al–2Nb is displayed in **Figure 3**a. The Fe–Al matrix (disordered A2 at forging temperature[20]) recrystallizes during forging with grains being approximately 4 μm in size. Recrystallization is completed for forging at 900 °C (and also higher temperatures, not shown here) in the head of the blade section (see Figure 1b) due to significantly higher total true strain in the order of 2.0 as compared to the root section. In the latter, the true strain remains in the order of 0.5, and, therefore, only partial recrystallization is found for forging at 900 °C. A deformed Fe–Al matrix persists in these regions under these conditions.

The Laves phase is predominantly found at grain boundaries of the (recrystallized) Fe–Al matrix in the form of individual particles. Former intergranular Laves phase from the as-cast microstructure can still be identified after the forging process by its characteristic, chain-like morphology (compare to Figure 2a). The continuity of the intergranular Laves phase from the as-cast state is disrupted by the forging process. During the forging process at 900 °C, the Laves phase fraction increases compared to the as-cast state. A maximum amount of Laves phase of about (7.8 ± 0.6) vol% is observed for forging at 900 °C.

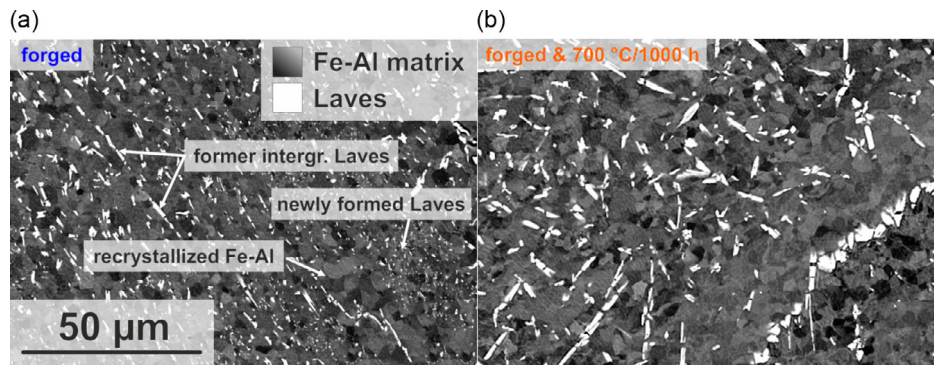That forging can be successfully employed to break up an existing network of Laves phase has been demonstrated for

Figure 3. SEM-BSE micrographs of the Fe–25Al–2Nb microstructure subsequent to (a) forging at 900 °C (head section in Figure 1b) and (b) 700 °C/1000 h following the forging at 900 °C (also head section). The micrographs were taken at the same magnification.

Fe–15Al–5Nb elsewhere.[26] The cast alloy of ref.[26] consisted of coarse α(Fe, Al) grains separated by a network of eutectic α (Fe, Al) and Laves phase. After hot forging at 1150 °C to a total strain of 6.0, a relatively homogeneous distribution of 19 vol% of equiaxed Laves phase particles with an average size of 1 μm was obtained, and the initial size of α(Fe, Al) was reduced from 250 to 10 μm.

A long-term annealing of forged Fe–25Al–2Nb for 1000 h at a potential application temperature of 700 °C (B2-ordered at heat treatment temperature[20]) in Figure 3b indicates no substantial coarsening of the Fe–Al subgrains. Image analysis yields a Laves phase fraction of (8.5 $\pm$ 0.5) vol%, which is insignificantly higher than for the forged condition (forging temperature of 900 °C). A slight increase is reasonable considering a decreasing solubility of the Fe–Al matrix for Nb with decreasing temperature.[20] That these forged microstructures are rather insensitive against coarsening was also found for Fe–15Al–5Nb, where no marked coarsening of the α(Fe, Al) grains was observed after creep testing at 700 °C for more than 100 h.[26]

Orientation imaging microscopy of the as-cast condition in **Figure 4**a expectedly reveals the formation of high-angle grain boundaries (HAGB) with intragrain point-to-point misorientation as low as 0.3°, as depicted in Figure 4c. These HAGB are still present in the forged material in Figure 4b (black arrows), but additional subgrains with low angle grain boundaries (LAGB) of 2°–15° misorientation have formed.

3.2. Quasistatic Deformation at Ambient and Elevated Temperatures

The samples from different preforms and from different positions within the parts did not show any systematic differences in mechanical testing, irrespective of the slight differences in microstructures due to varying cooling rates. Hence, they are not further distinguished in the following.

In **Figure 5**a, selected compressive stress-strain curves at different temperatures are shown for the cast and forged materials condition. In Figure 5b, the 1%-offset yield strengths extracted from the compression test data are summarized for temperatures between RT and 800 °C. Due to rather coarse grain sizes as compared to the cross-section tested in the mechanical tests,
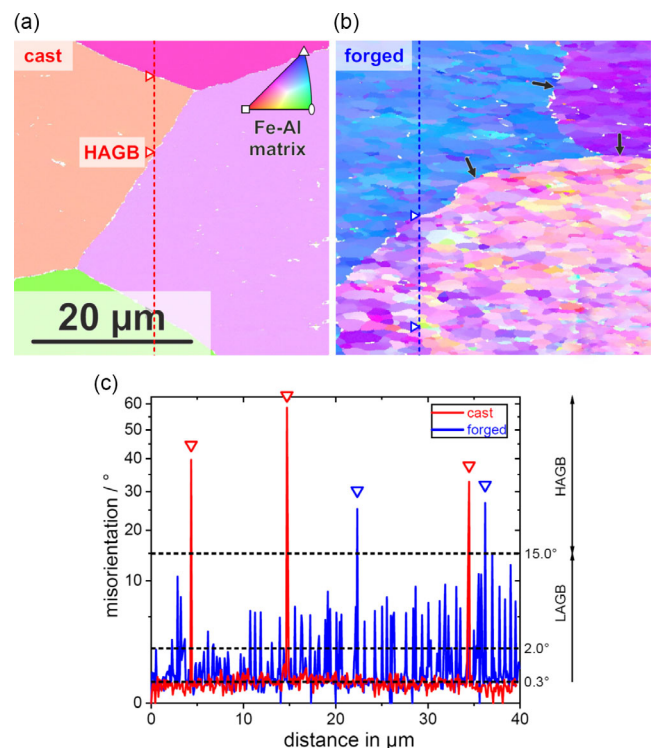

Figure 4. Orientation mapping according to the inverse pole figure of the sample surface normal (inset in a) for the Fe–Al matrix of Fe–25Al–2Nb (both from the head section according to Figure 1): (a) as-cast material (compare to Figure 2a) and (b) material forged at 900 °C (compare to Figure 3a). The micrographs were taken at the same magnification. Laves phase is detected during the scan but omitted in the maps and appears white. Vertical lines indicate the positions of the misorientation profiles in (c). Triangles indicate the positions (in (a,b)) and misorientations (in (c)) of HAGB (>15°). Note that the grain interior of the as-cast microstructure exhibits misorientations of max. 0.3° while the forged condition contains LAGB (2°–15°).

a 1% criterion was chosen to avoid scatter by differences in yielding and slight localization of plastic deformation in the early stages of testing. As the 400 °C/168 h annealing treatment to minimize the vacancy concentration had no systematic effect
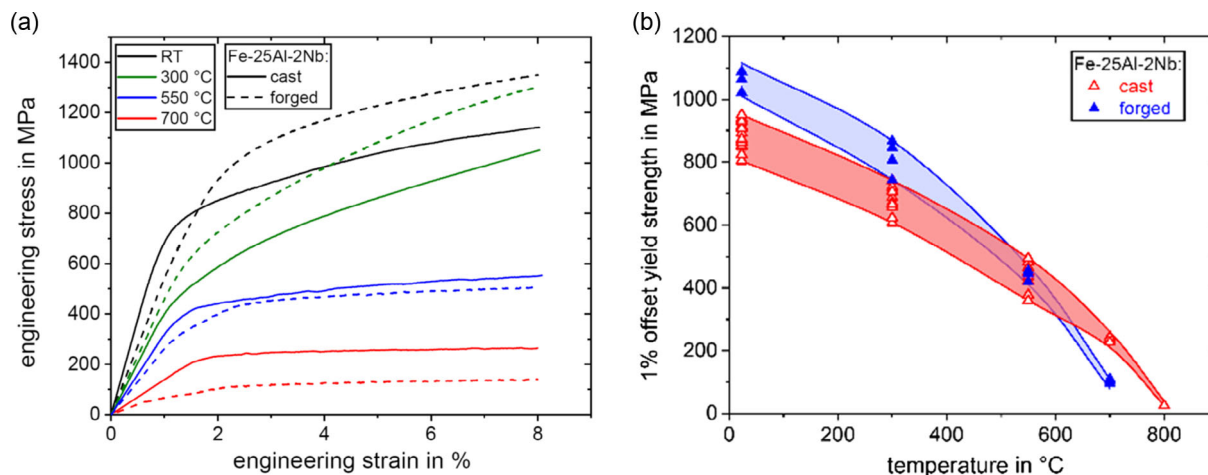
Figure 5. Compression test results at an initial strain rate of $10^{-4}\,\mathrm{s}^{-1}$ of the cast and forged Fe–25Al–2Nb: (a) some selected engineering stress-strain curves and (b) temperature dependence of the 1% offset yield strength determined from the compression tests.

on the determined yield strength, the results of these additionally annealed specimens are also not further distinguished in Figure 5b and in the following.

At RT and 300 °C, samples show higher strength in the forged state than in the cast condition. The higher volume fraction of Laves phase in the forged condition is not expected to lead to this significantly higher strength as the precipitates are mostly located at (sub)grain boundaries and rather coarse. Contrary, a higher Laves phase volume fraction is associated with a lower solid solution strengthening contribution due to a lower Nb level dissolved in the Fe–Al matrix. Consequently, the higher strength in the forged condition is attributed mainly to Hall–Petch strengthening because of the significantly smaller (sub)grain sizes, e.g., 280–550 μm in the cast state vs. 4 μm (sub)grain size in the forged condition. Apart from this, dislocation strengthening might also contribute to strength subsequent to the forging process. However, the even contrast in the recrystallized (sub) grains in Figure 3a indicates a rather low dislocation density within the subgrains but dislocation accumulation in subgrain boundaries. That yield strength increases at lower test temperatures when the grains have recrystallized after forging has also been found for Fe–25Al–2Ta.[11]

At 550 °C, there is no difference in the yield strength between the cast and forged state. However, at the potential application temperature of 700 °C, the as-cast condition shows higher strength than the forged condition. A lower scatter of yield strength (similar numbers of samples were tested at all temperatures), a lower strength at smaller grain size, and a significant drop in strength above 700 °C indicate a significant impact of diffusion-controlled deformation processes already being active during yielding at rather low plastic strains.

In **Figure 6**a, the offset yield strength of the laboratory Fe–25.7Al–2Nb reference alloy subsequent to 700 °C/1000 h is compared to Fe–25Al–2Ta (1000 °C/200 h) as a benchmark from the literature.[14] The strength of the reference alloy is slightly lower than that of the benchmark alloy throughout the temperature range tested. In Figure 6b, the Fe–25.7Al–2Nb reference alloy is compared to the industrially manufactured

Fe–25Al–2Nb alloy by its 1% offset yield strength. At RT, the reference alloy is close to the as-cast condition of Fe–25Al–2Nb due to a similar microstructural mockup. The forged conditions of Fe–25Al–2Nb exhibit higher RT strength mainly due to grain boundary strengthening. At high temperatures, strength of the reference alloy Fe–25.7Al–2Nb (700 °C/1000 h) is closer to the strength of the forged condition of Fe–25Al–2Nb.

In **Figure 7**a–c, the micrographs of the microstructures of the Fe–25Al–2Nb samples from the cast condition after compression tests at RT, 700 and 900 °C are displayed for comparison. Samples tested at RT (Figure 7a, D0$_3$-ordered at test temperature[20]) and 700 °C (Figure 7b, B2-ordered at test temperature[20]) show localized deformation in SEM-BSE micrographs. At 900 °C (and above, not shown here), dynamic recrystallization occurs (Figure 7c, disordered A2 at test temperature[20]), and newly formed grain boundaries can be identified. Some are partially pinned by the Laves phase particles. To differentiate the effect of deformation at higher temperatures on the microstructure, as-cast Fe–25Al–2Nb samples were heat treated without load under identical heating and cooling conditions. The microstructure of the heat-treated sample given in Figure 7d proves that it is not recrystallized at 900 °C.

Apart from grain nucleation and growth, the fraction of the Laves phase changes at temperatures above 700 °C, see **Figure 8**. At 800 °C, a maximum volume fraction of approximately (8.0 ± 0.8) vol% is obtained. Considering the uncertainty of the data, this is in agreement with the reported 7.4 vol% suggested by the application of the lever rule on the composition of the individual phases after long-term annealing for 1000 h at 700 °C in Fe–25.7Al–2Nb.[20] Above 800 °C, a continuously decreasing volume fraction of the Laves phase is noted, suggesting an increasing solubility of Nb in the Fe–Al matrix with increasing temperature.

3.3. Creep Deformation at 700 °C

In **Figure 9**a, creep curves at 80 MPa and 700 °C (B2-ordered at test temperature[20]) are comparatively displayed for the as-cast
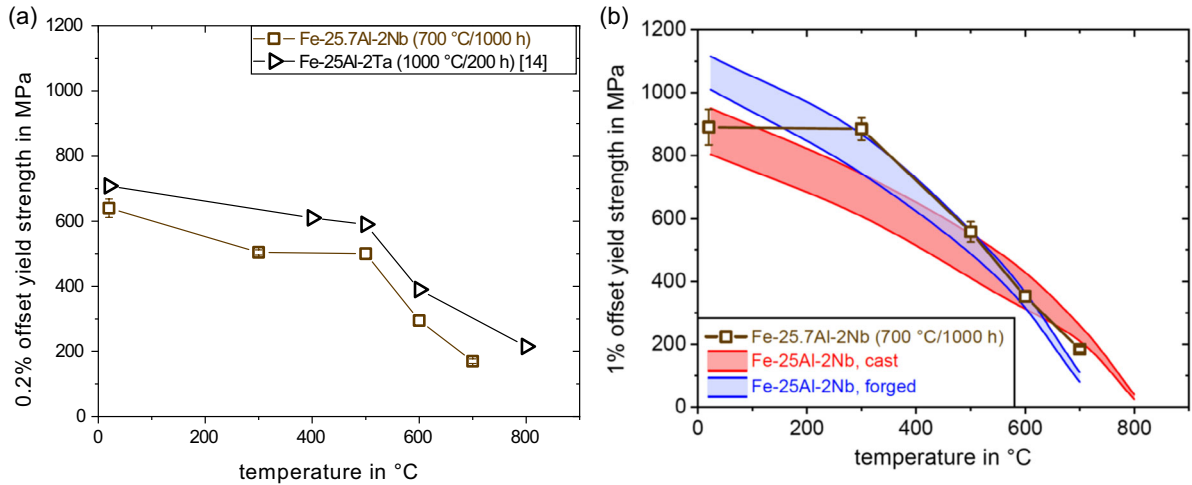
Figure 6. Compilation of compression strength data: (a) 0.2% offset yield strength of the laboratory Fe–25.7Al–2Nb reference alloy (700 °C/1000 h) and benchmark Fe–25Al–2Ta (1000 °C/200 h) from the literature[14] and (b) 1% offset yield strength of processed Fe–25Al–2Nb alloy from Figure 5b and the laboratory Fe–25.7Al–2Nb reference alloy (700 °C/1000 h). All data were obtained at an initial strain rate of 10^{-4} s^{-1}.
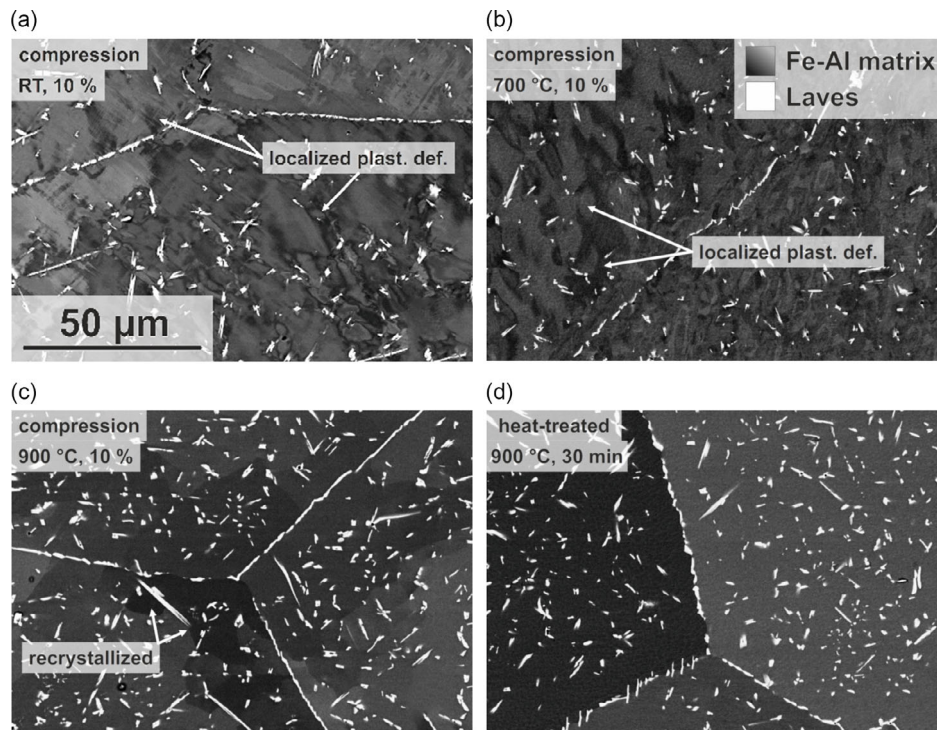

Figure 7. SEM-BSE micrographs of as-cast Fe–25Al–2Nb a–c) after compression testing up to 10% engineering strain and d) after an heat treatment for an equivalent time at 900 °C without mechanical load. All samples were taken from the head section as indicated in Figure 1a. The compression direction is vertical. Test temperatures are (a) RT, (b) 700 °C, and (c) 900 °C. The micrographs are taken at the same magnification. Arrows indicate localized deformation in (a,b) and new grains in (c).

and forged condition of the industrially manufactured Fe–25Al–2Nb. In the cast state (red curve), the true strain rate first decreases, passes through a minimum, and subsequently increases with increasing time and strain. The true strain rate of the forged material (blue curve) decreases monotonically with increasing time and strain and levels off at strains above 15%. The stress dependence of the strain rate at a true strain of

15% is used to compare both conditions in a double logarithmic representation of creep rate versus stress in Figure 9b. In addition, the minimum strain rate for the as-cast state is included as well. The apparent stress exponent n is determined according to Norton power law of creep, as presented in Equation (4). The apparent stress exponent n is 2.5 for the minimum strain rate and 2.6 for the strain rate at a strain of 15% of the as-cast state.

**ADVANCED
SCIENCE NEWS**

www.advancedsciencenews.com

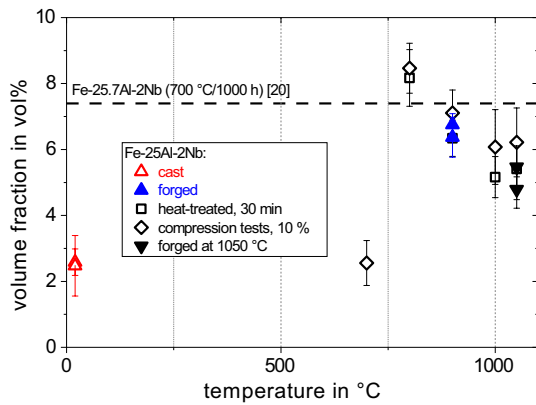**ADVANCED
ENGINEERING
MATERIALS**

www.aem-journal.com

Figure 8. Volume fraction of Laves phase as a function of temperature obtained from image analysis of various processing and testing conditions of Fe–25Al–2Nb.

Both apparent stress exponents are similar, indicating similar creep mechanisms active in the two creep stages. However, significant microstructural changes are present, contradicting this expectation, as shown below. The forged condition shows a significantly higher apparent stress exponent of 5.4, suggesting a different creep mechanism.

Long-term annealing of the cast microstructure (700 °C/1000 h) also leads to a significant change in creep behavior, as seen in Figure 9a (green curve). A similar creep behavior as compared to the forged condition (blue curve in Figure 9a) is obtained. The apparent stress exponent n increases to 6.6, similarly high as for the forged condition ($n = 5.4$). In contrast to the forged material, a significantly lower strain rate at 15% strain is detected in agreement with the much larger grain size of this condition compared to the forged material. It is worth noting that the determined strength values from the quasistatic compression tests at 700 °C (see Figure 5b) match the stresses obtained by

extrapolation of the creep data to $10^{-4}\,s^{-1}$, e.g., 245 and 110 MPa for the cast and forged condition, respectively.

Comparison to the tensile creep data of the laboratory Fe–25.7Al–2Nb–0.01B reference alloy (700 °C/1000 h) shows that the alloy exhibits a comparable steady-state creep rate and stress exponent as obtained for the forged and the long-term annealed Fe–25Al–2Nb after industrial manufacturing. Similar to the forged Fe–25Al–2Nb, no minimum but a steady state creep rate is obtained. The creep strength of Fe–25Al–2Nb alloy is considerably lower than that of the benchmark Fe–25Al–2Ta alloy (1000 °C/200 h; the statement is also valid for forged Fe–25Al–2Ta). The extrapolation of the reported creep rates of Fe–25Al–2Ta at 700 °C to $10^{-4}\,s^{-1}$ leads to higher stresses than the strength depicted in Figure 6a for quasistatic tests. However, the extrapolation is performed over a much wider strain rate range in comparison to Fe–25Al–2Nb, and thus, overestimation due to assuming a constant rather than an increasing stress exponent is to be expected (decreasing contribution of diffusion creep deformation; increasing contribution of dislocation climb controlled creep).

To analyze the complex creep behavior with a pronounced minimum creep rate in the case of the Fe–25Al–2Nb as-cast state, the changes in microstructure during creep were studied. One creep test was stopped at the minimum creep rate, which was attained after 4 h. It is compared to the microstructure of a sample that crept to a strain of 15% which was reached after 22 h of creep. The microstructures of both samples are displayed in **Figure 10**.

The microstructure of the sample at a minimum creep rate (after 4 h) exhibits significant localized plastic deformation, see Figure 10a. In the high-resolution micrograph in Figure 10b, fine, needle- or plate-like precipitates are seen in the Fe–Al matrix, similar to what is expected for the coherent precipitation of the $L2_1$ Heusler phase.[9] As a result of Nb depletion, no Heusler phase is found in the vicinity of the coarser Laves phase particles.
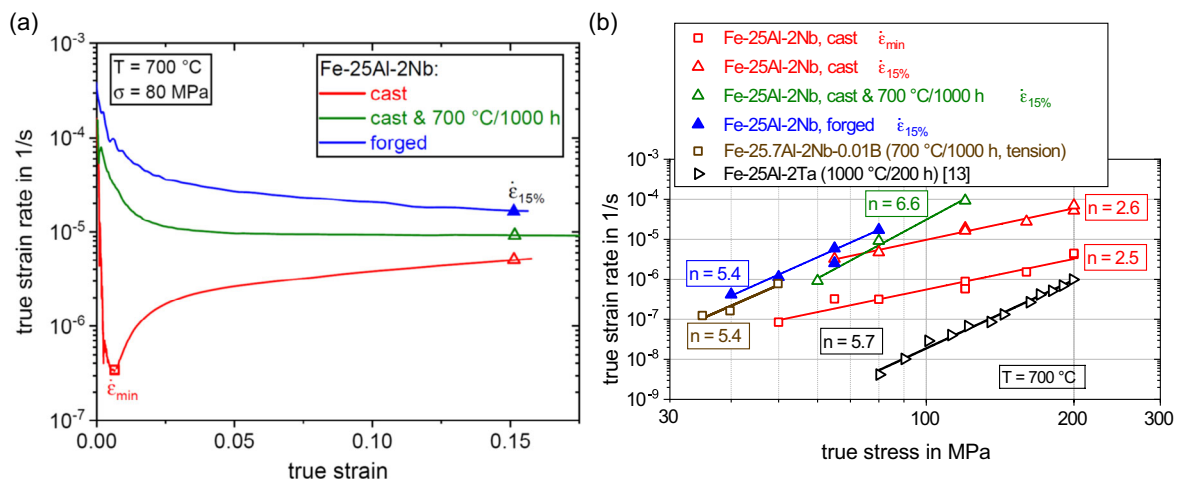

Figure 9. (a) Compression creep response of Fe–25Al–2Nb in different conditions tested at 700 °C and 80 MPa. (b) Stress dependence of true strain rate at a strain of 15%. In addition, the stress dependence of the minimum strain rate is also included for the as-cast state. Furthermore, tensile creep results of the laboratory Fe–25.7Al–2Nb–0.01B are included in (b), along with results from step-wise compressive creep tests from the literature on the benchmark Fe–25Al–2Ta.[13]

**ADVANCED
SCIENCE NEWS**

www.advancedsciencenews.com

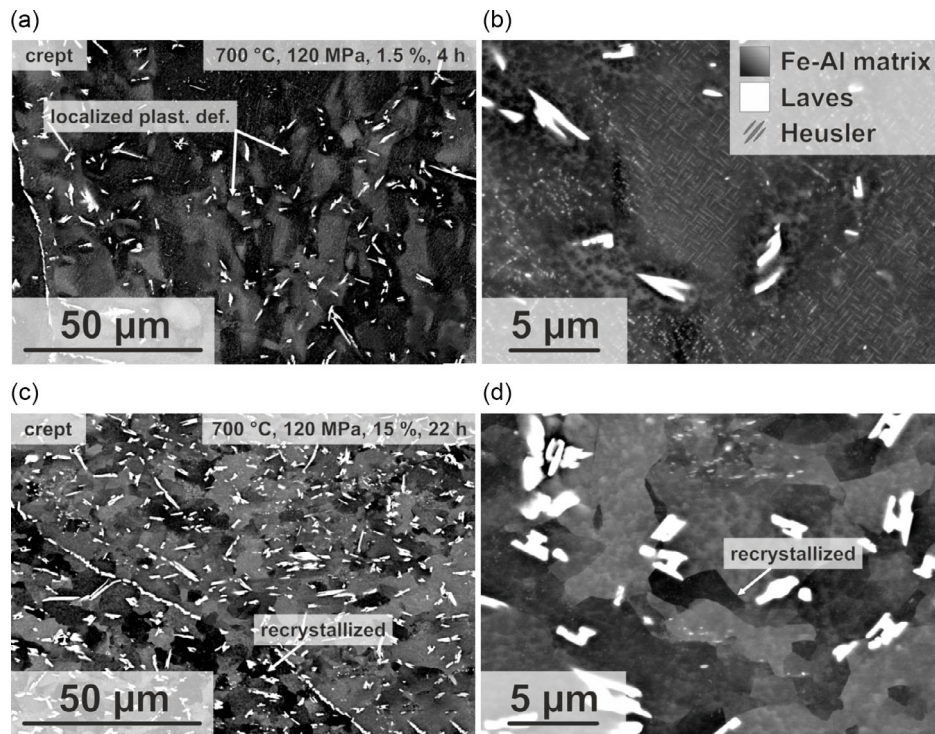**ADVANCED
ENGINEERING
MATERIALS**

www.aem-journal.com

Figure 10. SEM-BSE micrographs of cast Fe–25Al–2Nb specimens subjected to creep deformation at 700 °C/120 MPa: a,b) minimum strain rate after 4 h and c,d) a true strain of 15% after 22 h. The micrographs (a,c) and (b,d) are taken at the same magnification each. The compression direction is vertical. Arrows indicate localized plastic deformation in (a) and new grains in (c,d). Heusler phase is seen as faint needle- or plate-like features in (b).

The microstructure of the sample after a strain of 15% (22 h) is recrystallized, see Figure 10c. In the detailed image of the microstructure in Figure 10d, small precipitates can be found as white particles with no obvious orientation relationship with each other or to the Fe–Al matrix. These precipitates are Laves phase formed after the dissolution of the Heusler phase. According to the lower Nb content of the Heusler phase, the regions with these small particles after 22 h of creep deformation are of a lesser extent than the regions of the Heusler phase obtained after 4 h of creep deformation.

As far as the creep response of the as-cast condition is concerned, the early formation of coherent Heusler phase might contribute to significant strengthening and, hence, drop in creep rate. Beyond the minimum, loss in coherence, ripening, and dissolution might lead to softening and a continuous increase of creep rate over time and strain. This might be facilitated by subgrain formation observed in Figure 10c,d.

To distinguish the effect of creep deformation at 700 °C from the effect by thermal treatment on the formation and transformation of the Heusler phase, some samples were heat treated at 700 °C for 1, 4, and 22 h (B2-ordered at heat treatment temperature[20]). The micrographs after heat treatment are given in **Figure 11**. After 1 h of heat treatment, Heusler phase precipitates can already be identified in the matrix, which become more distinct after 4 h. After 22 h of heat treatment (Figure 11c), Heusler phase precipitates can still be seen as lenticular, most probably coherent features, as after 4 h of heat treatment (Figure 11b) and in contrast to 22 h of creep (Figure 10c). The evolution of the

microstructure in Fe–24Al–2Nb–0.01B at 700 °C for durations up to 1000 h was studied elsewhere.[23] Heusler phase formation was also confirmed after 1 and 10 h at 700 °C, while no Heusler phase was observed after 100 h.[22] Observation of the Heusler phase after 4 and 22 h in the current alloy is, thus, in agreement with these findings.

The results prove that the dissolution of the Heusler and precipitation of the Laves phase at 700 °C is accelerated by creep deformation. With increasing deformation, the nucleation rate might increase due to the presence of dislocations as nucleation sites, and additionally, the coherence of the Heusler phase with the Fe–Al matrix disappears, which may be a necessary prerequisite for the occurrence of metastable Heusler phase. Both result in the acceleration of the transformation of the metastable Heusler phase. Hence, the Heusler phase is more pronounced in the matrix after 22 h of heat treatment than after 22 h of creep deformation at the same temperature.

The phase formation (Heusler and Laves) proceeds significantly slower and more homogeneous in the Fe–25Al–2Ta benchmark alloy (see Figure 5b,c in ref.[13]). This might be the main contribution to its superior creep resistance due to hindering dislocation motion. The effective strengthening potential of the Heusler phase, for example, in this respect, was proven in the present investigation for the as-cast condition of Fe–25Al–2Nb. Recrystallization as another contribution to creep deformation obtained by orientation contrast imaging in Fe–25Al–2Nb might also be more pronounced as a consequence of lesser and coarser precipitates. However, no
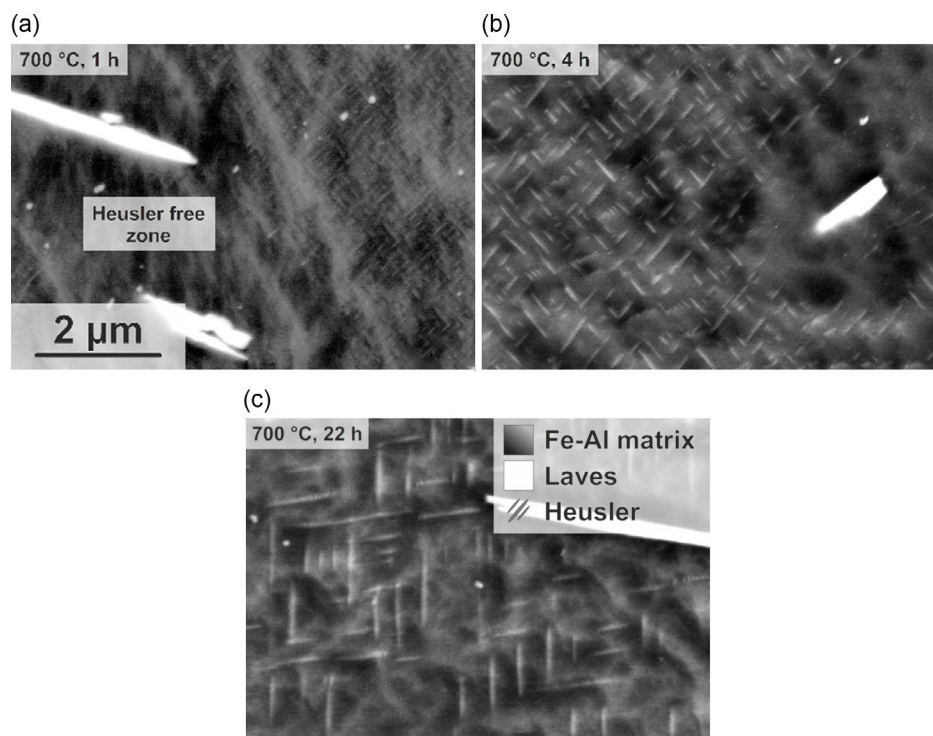
Figure 11. SEM-BSE micrographs of cast Fe–25Al–2Nb (head section according to Figure 1a) heat-treated at 700 °C for (a) 1 h, (b) 4 h, and (c) 22 h. Heusler phase is absent in the vicinity of Laves phase due to Nb depletion. All micrographs are taken at the same magnification.

detailed orientation images are available for the Fe–Al–Ta alloy in the literature to further assess this contribution to creep deformation.

4. Conclusions

Based on the performed investigations following conclusions can be drawn: 1) Fe–Al–Nb alloys with Fe_3Al matrix and Laves phase precipitates can be manufactured on an industrially relevant scale; 2) The mechanical strength of the Fe–Al–Nb is lower as compared to Ta-containing variants. At low temperatures, it is governed mainly by grain size. At high temperatures, Laves phase fraction and its distribution in the Fe–Al matrix is decisive. Considering the lower costs and density of the Nb-containing alloys, the lower strength appears acceptable; 3) Creep behavior is complex for the nonequilibrium as-cast condition as a transient Heusler phase is formed in the early stages of creep, leading to a significant strengthening. Its dissolution and the formation of Laves phase as well as the occurrence of recrystallization, lead to the acceleration of creep in the later stages of creep; and 4) Forging results in a refinement of the coarse as-cast microstructure, further precipitation of Laves phase, and a creep behavior similar to the one obtained in close-to-equilibrium Fe–25Al–2Nb.

Conflict of Interest

The authors declare no conflict of interest.

Data Availability Statement

The data presented in this study are available in KITopen at https://doi.org/10.5445/IR/1000157792 under CC BY-SA 4.0 license. Further information is available upon request with alexander.kauffmann@kit.edu.

[1] C. G. McKamey, in: N. S. Stoloff, V.K. Sikka (Eds.), *Physical Metallurgy and Processing of Intermetallic Compounds*, Chapman Hall/Springer, Boston, MA, **1996**, pp. 351-391.

[2] M. Palm, F. Stein, G. Dehm, *Ann. Rev. Mater. Res.* **2019**, *49*, 297.

[3] D. Hardwick, G. Wallwork, *Rev. High Temp. Mater.* **1978**, *4*, 47.

[4] V. K. Sikka, in *Processing, Properties, and Applications of Iron Aluminides* (Eds: J. H. Schneibel, M.A. Crimp), TMS, Warrendale, **1994**, pp. 3-18.

[5] D. G. Morris, M. A. Muñoz-Morris, *Adv. Eng. Mater.* **2011**, *13*, 43.

[6] M. Palm, A. Schneider, F. Stein, G. Sauthoff, *MRS OPL* **2005**, *842*, 3.

[7] M. Palm, *Int. J. Mater. Res.* **2009**, *100*, 277.

[8] D. G. Morris, M. A. Muñoz-Morris, C. Baudin, *Acta Mater.* **2004**, *52*, 2827.

[9] D. G. Morris, L. M. Requejo, M. A. Muñoz-Morris, *Intermetallics* **2005**, *13*, 862.

[10] D. G. Morris, M. A. Muñoz-Morris, L. M. Requejo, *Acta Mater.* **2006**, *54*, 2335.

[11] P. Hanus, E. Bartsch, M. Palm, R. Krein, K. Bauer-Partenheimer, P. Janschek, *Intermetallics* **2010**, *18*, 1379.

[12] P. Prokopčáková, M. Švec, M. Palm, *Int. J. Mater. Res.* **2016**, *107*, 396.

[13] D. D. Risanti, G. Sauthoff, *Intermetallics* **2011**, *19*, 1727.

[14] D. D. Risanti, G. Sauthoff, *Intermetallics* **2005**, *13*, 1313.

[15] D. M. Dimiduk, M. G. Mendiratta, D. Banarjee, H. A. Lipsitt, *Acta Metallurgica* **1988**, *36*, 2947.

[16] A. Malfliet, F. Stein, T. Vaubois, K. C. Hari Kumar, Materials Science International Team, *Al-Fe-Nb Ternary Phase Diagram Evaluation Phase diagrams, crystallographic and thermodynamic data: Datasheet from MSI Eureka in Springer Materials*, MSI Materials Science International Services GmbH.

[17] M. Palm, *J. Alloys Compd.* **2009**, *475*, 173.

[18] F. Stein, C. He, O. Prymak, S. Voß, I. Wossack, *Intermetallics* **2015**, *59*, 43.

[19] O. Prymak, F. Stein, *Intermetallics* **2010**, *18*, 1322.

[20] A. Gedsun, F. Stein, M. Palm, *J. Phase Equilibria Diffus.* **2022**, *43*, 409.

[21] S. A. Azmi, A. Michalcová, L. Senčekova, M. Palm, *MRS Adv.* **2017**, *2*, 1353.

[22] A. Gedsun, S. Antonov, T. S. Prithiv, M. Palm, *Scr. Mater.* **2023**, *226*, 115220.

[23] A. Gedsun, F. Stein, M. Palm, *MRS Adv.* **2021**, *6*, 176.

[24] G. Dlubek, O. Brümmer, B. Möser, *Cryst. Res. Technol.* **1982**, *17*, 951.

[25] J. Čížek, F. Lukáč, O. Melikhova, I. Procházka, R. Kužel, *Acta Mater.* **2011**, *59*, 4068.

[26] D. G. Morris, M. A. Muñoz-Morris, *Mater. Sci. Eng. A* **2012**, *552*, 134.